ACS NANO
Cite This: *ACS Nano* 2018, 12, 12492−12502
www.acsnano.org

Atomic Substitution Enabled Synthesis of Vacancy-Rich Two-Dimensional Black TiO_{2-x} Nanoflakes for High-Performance Rechargeable Magnesium Batteries

Yanrong Wang,[†] Xiaolan Xue,[†] Pingying Liu,[‡] Caixing Wang,[†] Xu Yi,[†] Yi Hu,[†] Lianbo Ma,[†] Guoyin Zhu,[†] Renpeng Chen,[†] Tao Chen,[†] Jing Ma,*[,†] Jie Liu,[†,§] and Zhong Jin*[,†]

[†] Key Laboratory of Mesoscopic Chemistry of MOE, School of Chemistry and Chemical Engineering, Nanjing University, Nanjing, Jiangsu 210023, China

[‡] School of Materials Science and Engineering, Jingdezhen Ceramic Institute, Jingdezhen 333403, China

[§] Department of Chemistry, Duke University, Durham, North Carolina 27708, United States

Supporting Information

ABSTRACT: **Rechargeable magnesium (Mg) batteries assembled with dendrite-free, safe, and earth-abundant metal Mg anodes potentially have the advantages of high theoretical specific capacity and energy density. Nevertheless, owing to the large polarity of divalent Mg^{2+} ions, the insertion of Mg^{2+} into electrode materials suffers from sluggish kinetics, which seriously limit the performance of Mg batteries. Herein, we demonstrate an atomic substitution strategy for the controlled preparation of ultrathin black TiO_{2-x} (B-TiO_{2-x}) nanoflakes with rich oxygen vacancies (OVs) and porosity by utilizing ultrathin 2D TiS_2 nanoflakes as precursors. We find out that the presence of OVs in B-TiO_{2-x} electrode material can greatly improve the electrochemical performances of rechargeable Mg batteries. Both experimental results and density functional theory simulations confirm that the introduction of OVs can remarkably enhance the electrical conductivity and increase the number of active sites for Mg^{2+} ion storage. The vacancy-rich B-TiO_{2-x} nanoflakes exhibit high reversible capacity and good capacity retention after long-term cycling at large current densities. It is hoped that this work can provide valuable insights and inspirations on the defect engineering of electrode materials for rechargeable magnesium batteries.**

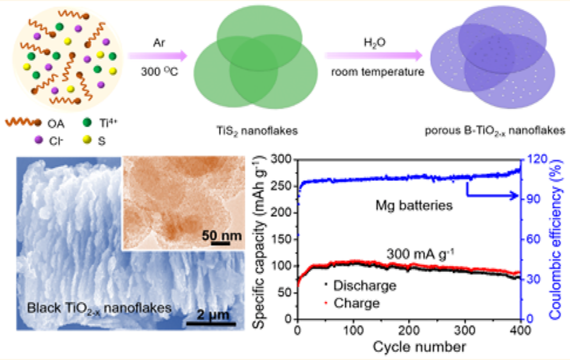

KEYWORDS: *rechargeable magnesium batteries, anode material, oxygen vacancies, black* TiO_{2-x}*, porous nanoflakes*

Rechargeable batteries based on multivalent ions with sustainable resources, low cost, and high safety present a promising future prospect for next-generation large-scale energy storage.[1−4] Among them, magnesium (Mg) batteries have attracted considerable attention due to the earth abundance of Mg metal, large volumetric theoretical energy density (3833 mAh cm^{-3}), and free of dendrite growth on cycling.[5,6] Whereas the development of rechargeable Mg batteries has been hampered by two dominating intrinsic challenges, the first obstacle is the lack of appropriate electrolyte allowing reversible Mg plating/stripping with specific stable operating voltage windows.[7] Another obstacle is the sluggish diffusion kinetics of Mg^{2+} ions in electrode materials originated from the strong electrostatic interactions between highly polarized divalent Mg^{2+} ions and the crystalline lattices of electrode materials.[8,9] Since 2000, great efforts have been made to search for compatible electrolytes as well as advanced electrode materials with suitable potential, high capacity, long cyclicity, and fast kinetics for Mg batteries.[10−18] So far, only a few metal/alloy-type and ion insertion-type negative electrode materials have been found to exhibit reasonable discharge/charge capacity and cycling durability in rechargeable Mg batteries.[4,19−23]

Crystal defects, such as oxygen vacancies (OVs), play a vital role in the physicochemical properties of transition-metal oxides. The presence of OVs can improve the electronic conductivity of transition-metal oxides for the application in

Received: September 10, 2018
Accepted: November 26, 2018
Published: November 26, 2018

DOI: 10.1021/acsnano.8b06917
ACS Nano 2018, 12, 12492−12502

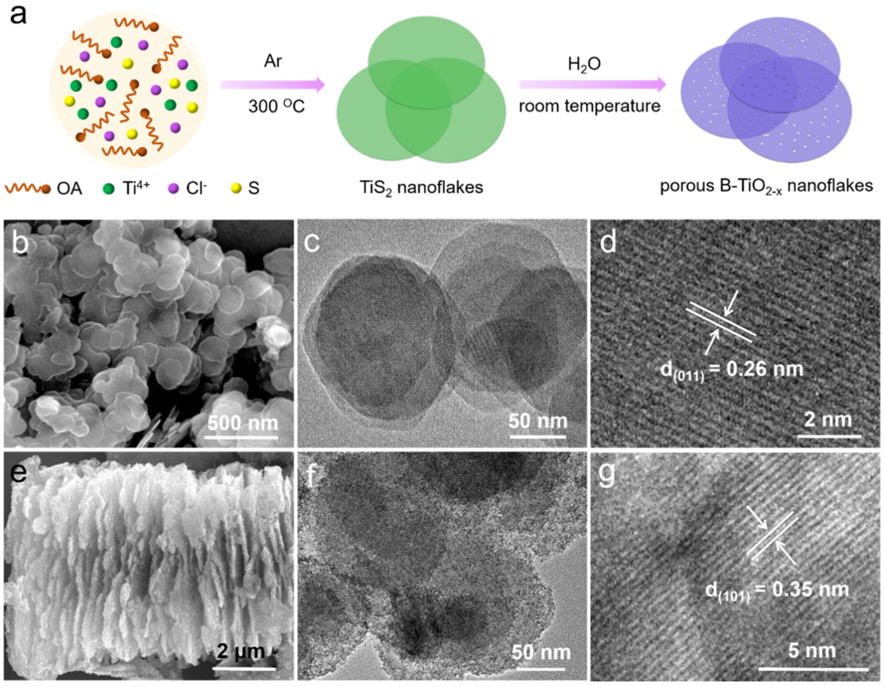

Figure 1. Schematic synthesis process of B-TiO_{2-x} nanoflakes and morphology characterizations of samples. (a) Schematic synthesis process of OVs-rich and porous B-TiO_{2-x} nanoflakes converted from ultrathin 2D TiS_2 nanoflakes through an atomic substitution strategy. SEM, TEM, and HRTEM images of (b−d) precursor TiS_2 nanoflakes and (d−f) as-obtained B-TiO_{2-x} nanoflakes.

catalysis, photoelectrolysis, and energy storage.[24−28] Especially, the OVs in the oxide-based electrode materials of Li-ion or Na-ion batteries can facilitate the electron and ion transport, thereby contributing to higher capacity and better rate performance.[29−34] For instance, it has been reported that the incorporation of OVs into TiO_{2-x} can reduce the band gap and raise the density of states below the Fermi level for TiO_2,[35−37] which is in favor of improving its electrical conductivity thus improving the electrochemical performance for Li-ion and Na-ion batteries.[38] However, as far as we know, the influence of OVs on the electrochemical performances of electrode materials in Mg batteries has been rarely investigated.

In this study, we report the atomic substitution conversion of ultrathin 2D TiS_2 nanoflakes into OVs-rich and porous black TiO_{2-x} (B-TiO_{2-x}) nanoflakes. We also demonstrate the enhancement effect of OVs on the magnesium energy storage of B-TiO_{2-x} nanoflakes, which brings improved reversible capacity, rate performance, and long cycle stability. The Mg^{2+} ions storage mechanism in B-TiO_{2-x} nanoflakes was investigated by systematic electrochemistry characterizations, *ex situ* characterizations, and theoretical calculations, revealing that both Mg^{2+} insertion process and capacitive response contribute to the capacity. This work indicates that the introduction of OVs into transition-metal oxide electrode materials could be an effective approach to engineering the electrode performance for rechargeable Mg batteries.

RESULTS AND DISCUSSION

Figure 1a shows the schematic diagram of the synthesis method of OVs-rich and porous B-TiO_{2-x} nanoflakes. Primarily, ultrathin 2D TiS_2 nanoflakes were obtained *via* the reaction of $TiCl_4$ and elemental S in the presence of oleylamine refluxed at 300 °C under N_2 protection condition, as detailed in the Experimental Section. The X-ray powder diffraction (XRD) pattern of TiS_2 nanoflakes (see Figure S1) shows strong diffraction peaks that can be well asssigned to the hexagonal phase of TiS_2 (JCPDS. PDF no. 88-1967, space group $P\overline{3}m1$, $a = b = 3.4073$ Å, $c = 5.6953$ Å). The OVs-rich B-TiO_{2-x} nanoflakes were simply synthesized by stirring the TiS_2 nanoflakes in water at room temperature for 72 h. During this step, the sulfur atoms in TiS_2 nanoflakes were substituted by oxygen atoms, generating reductive H_2S, and abundant OVs were formed during the atomic substation process, in which a part of the Ti^{4+} species was reduced to Ti^{3+} by the reductive H_2S. The scanning electron microscopy (SEM) and transmission electron microscopy (TEM) images shown in Figure 1b−g exhibit the morphology of precursor TiS_2 nanoflakes and as-obtained OV-rich B-TiO_{2-x} nanoflakes. The smooth TiS_2 nanoflakes have a uniform thickness of 5−10 nm and a diameter of 100−200 nm (Figure 1b,c). Most of the TiS_2 nanoflakes were spontaneously piled together for minimizing the surface energy. Moreover, the high-resolution TEM (HRTEM) image in Figure 1d shows a clear lattice spacing of 0.26 nm, which matches well with the (011) planes of hexagonal phase TiS_2. The as-prepared B-TiO_{2-x} nanoflakes are also stacked (Figure 1e), exhibiting rough and porous surface characteristics (Figure 1f). The porous surface was likely formed because the S^{2-} species in TiS_2 were replaced by smaller O^{2-} through an atomic substitution process. As shown in the HRTEM image of Figure 1g, the lattice spacing of 0.35 nm matches well with the (101) planes of tetragonal-phase anatase TiO_2. The presence of disordered regions in the crystalline lattice indicates the introduction of OVs.[36] We also prepared a control sample of fully oxidized and OVs-free white TiO_2 nanoflakes (W-TiO_2) by annealing the B-TiO_{2-x} nanoflakes in air atmosphere at 450 °C for 4 h. The morphology of W-TiO_2 control sample is shown in Figure S2, which well maintains the original morphology of B-TiO_{2-x} nanoflakes. The specific surface area and porous characteristics of B-TiO_{2-x} nanoflakes and W-TiO_2 control sample were

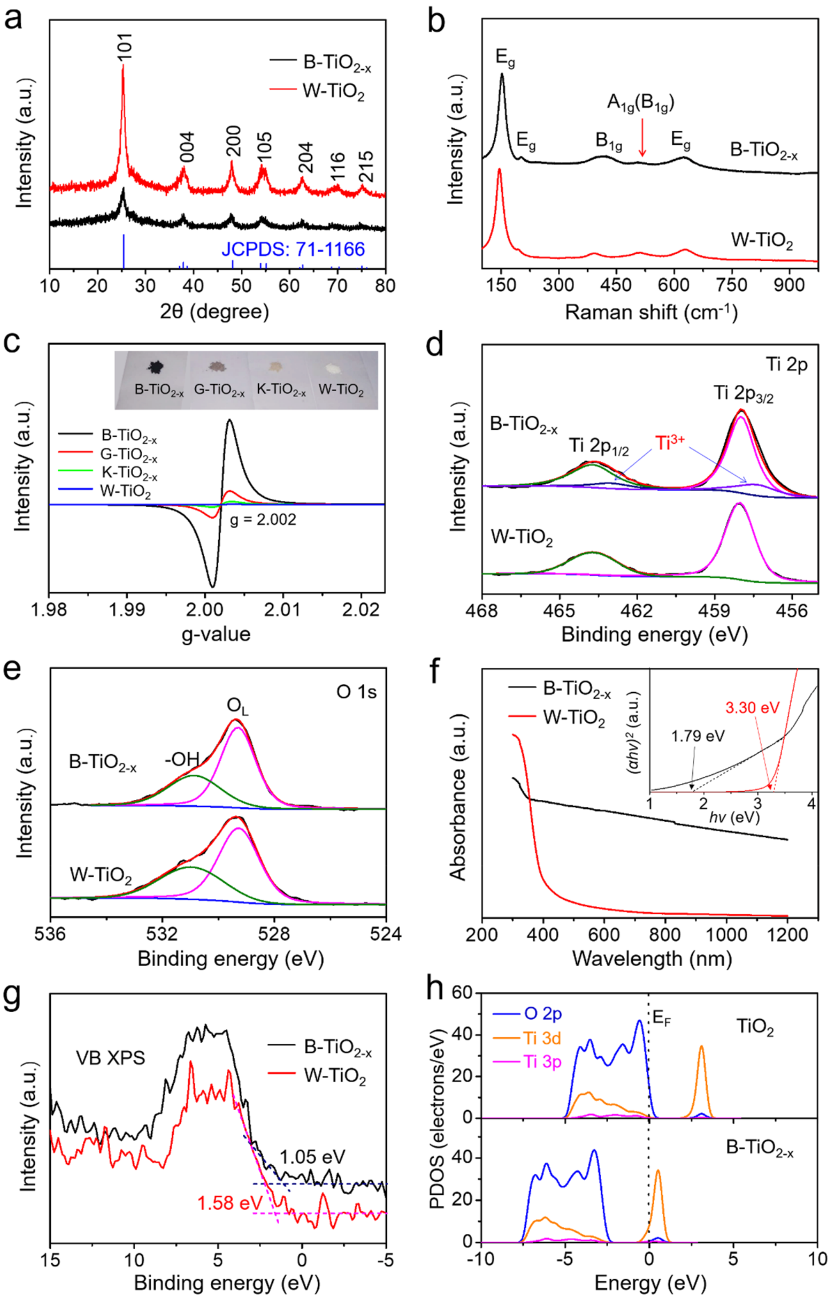

Figure 2. Characterizations of B-TiO_{2-x} and W-TiO_2 nanoflakes: (a) XRD patterns, (b) Raman spectra, (c) photographs and EPR spectra of B-TiO_{2-x} and other control samples prepared by annealing in air for different periods (G-TiO_{2-x} (annealed for 1 h), K-TiO_{2-x} (annealed for 2 h), W-TiO_2 (annealed for 4 h), respectively), (d, e) XPS spectra of (d) Ti 2p and (e) O 1s core levels, (f) UV–vis diffuse reflectance spectra and optical bandgaps, (g) valence-band X-ray photoelectron spectra of B-TiO_{2-x} nanoflakes and W-TiO_2 control sample. (h) The calculated PDOS of pristine TiO_2 and B-TiO_{2-x} with OVs.

investigated by N_2 adsorption–desorption isotherms (see Figure S3), revealing the high specific surface areas of *ca.* 134 and 139 $m^2\ g^{-1}$, respectively. The pore size distributions in Figure S3b,d demonstrate the bimodal micromesoporous structures in B-TiO_{2-x} and W-TiO_2.

The crystallinity structures of B-TiO_{2-x} and W-TiO_2 nanoflakes were examined by XRD (Figure 2a). The major XRD peaks of both samples can be indexed to tetragonal phase TiO_2 (JCPDS no. 71-1166, space group *I*41/*amd*, $a = b = 3.7842$, $c = 9.5146$). This result suggests the successful conversion of TiS_2 into B-TiO_{2-x}. The XRD pattern of B-TiO_{2-x} nanoflakes presents broader peaks with weaker diffraction intensities than those of W-TiO_2, which is due to the presence of abundant OVs.[39] The structural features of both samples were further examined by Raman spectroscopy. Six ($3E_g + 2B_{1g} + A_{1g}$) Raman-active modes (151.9, 200.9, 414.8, 506.9, 625.8 cm^{-1}) were detected in the B-TiO_{2-x} nanoflakes (Figure 2b).[40] The strongest E_g mode arisen from the external vibration of Ti–O bonds (151.9 cm^{-1}) has an obvious red shift compared to that of W-TiO_2 (145.4 cm^{-1}), which can be attributed to the increased amount of OVs in B-TiO_{2-x}.[26] Control samples with different OV contents were prepared by annealing the porous B-TiO_{2-x} nanoflakes at 450 °C in air for different periods (1, 2, or 4 h) to investigate the

DOI: 10.1021/acsnano.8b06917
ACS Nano 2018, 12, 12492−12502

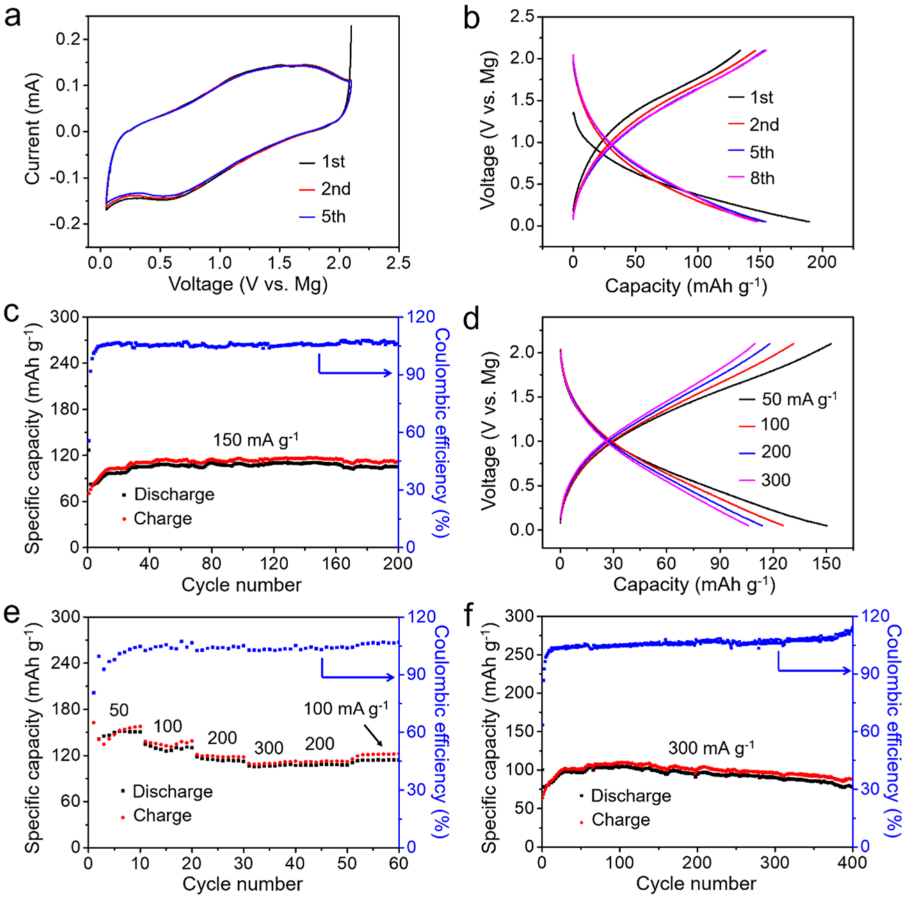

Figure 3. Electrochemical performances of porous B-TiO$_{2-x}$ nanoflakes cycling between 0.05−2.1 V *vs* Mg^{2+}/Mg. (a) CV curves at a scanning rate of 0.2 mV s^{-1}. (b) Discharge−charge curves at 50 mA g^{-1}. (c) Cycling performance and Coulombic efficiencies at 150 mA g^{-1}. (d) Discharge/charge curves at the different current densities ranged from 50 to 300 mA g^{-1}. (e) Rate performance and (f) cycling performance measured at 300 mA g^{-1}.

effects of OV contents in B-TiO$_{2-x}$ on Mg^{2+} storage performance. The inset of Figure 2c shows the colors of these control samples gradually change from black to gray (1 h), khaki (2 h), and finally white (4 h), and these control samples are termed as G-TiO$_{2-x}$, K-TiO$_{2-x}$, and W-TiO$_2$, respectively, which are associated with the decrease of OV contents. Electron paramagnetic resonance spectroscopy (EPR) was conducted on these control samples at room temperature to examine the existence of OVs, as shown in Figure 2c. The B-TiO$_{2-x}$, G-TiO$_{2-x}$, and K-TiO$_{2-x}$ nanoflakes show distinct EPR signals with a g value of 2.002, which indicates the presence of superoxide radicals ($O_2^{\bullet-}$) attached to the OVs on the surface of metal oxide materials.[31,37,40−42] Based on electron spin concentration measurements, the $O_2^{\bullet-}$ concentration in porous B-TiO$_{2-x}$ nanoflakes is estimated to be 0.57 μmol g^{-1}, which is significantly higher than that of a previous reported $O_2^{\bullet-}$ concentration (0.018 μmol g^{-1}).[43] The intensity of EPR signals is gradually reduced with prolonging annealing time, implying the decrease of OV content. After annealing for 4 h, the sample was fully oxidized to W-TiO$_2$ with very few OVs. XPS was further conducted to examine the elemental compositions and chemical states of samples (Figure 2d,e). The survey XPS spectrum of B-TiO$_{2-x}$ nanoflakes revealed the co-existence of Ti and O elements (see Figure S4a). Almost no peak of S was detected, indicating successful conversion of TiS$_2$ into B-TiO$_{2-x}$. The energy dispersive X-ray spectroscopy (EDX) elemental analysis of B-TiO$_{2-x}$ nanoflakes revealed the presence of very little S (see Figure S4b), which is consistent with the XPS results. The energy bands of B-TiO$_{2-x}$ nanoflakes at Ti 2p region can be deconvoluted to four peaks. The peaks located at 458.0 and 463.7 eV are assigned to Ti^{4+} 2p$_{3/2}$ and 2p$_{1/2}$, respectively. The peaks located at 457.3 and 463.0 eV are associated with Ti^{3+} 2p$_{3/2}$ and 2p$_{1/2}$, respectively.[44] The Ti^{3+} species were produced during the atomic substation process of S^{2-} with O^{2-}, in which the Ti^{4+} in TiO$_{2-x}$ was reduced by the generated reductive H$_2$S. In contrast, the W-TiO$_2$ nanoflakes only show two peaks at 458.0 and 463.7 eV, which are the typical characteristics of Ti^{4+}. The O 1s band of B-TiO$_{2-x}$ and W-TiO$_2$ nanoflakes in Figure 2e can be fitted into two peaks, corresponding to the lattice oxygen (O$_L$) in TiO$_{2-x}$ (~529.3 eV) and surface −OH group (~530.9 eV), respectively.[40,45]

The UV−vis diffuse reflectance spectra (Figure 2f) show that the photoabsorption of B-TiO$_{2-x}$ nanoflakes has been extended from UV light to visible light and infrared regions. The bandgap of B-TiO$_{2-x}$ nanoflakes was measured to be ~1.79 eV, which is much narrower than that of W-TiO$_2$ (~3.30 eV), as shown in the inset of Figure 2f. The narrowed optic bandgap might result from the additional impurity energy levels between conduction band (CB) and valence band (VB) introduced by Ti^{3+} species and OVs.[36,44] The VB XPS spectrum of B-TiO$_{2-x}$ nanoflakes (Figure 2g) show an absorption onset located at ~1.05 eV, while the absorption onset of W-TiO$_2$ shifts to ~1.58 eV, indicating the change of

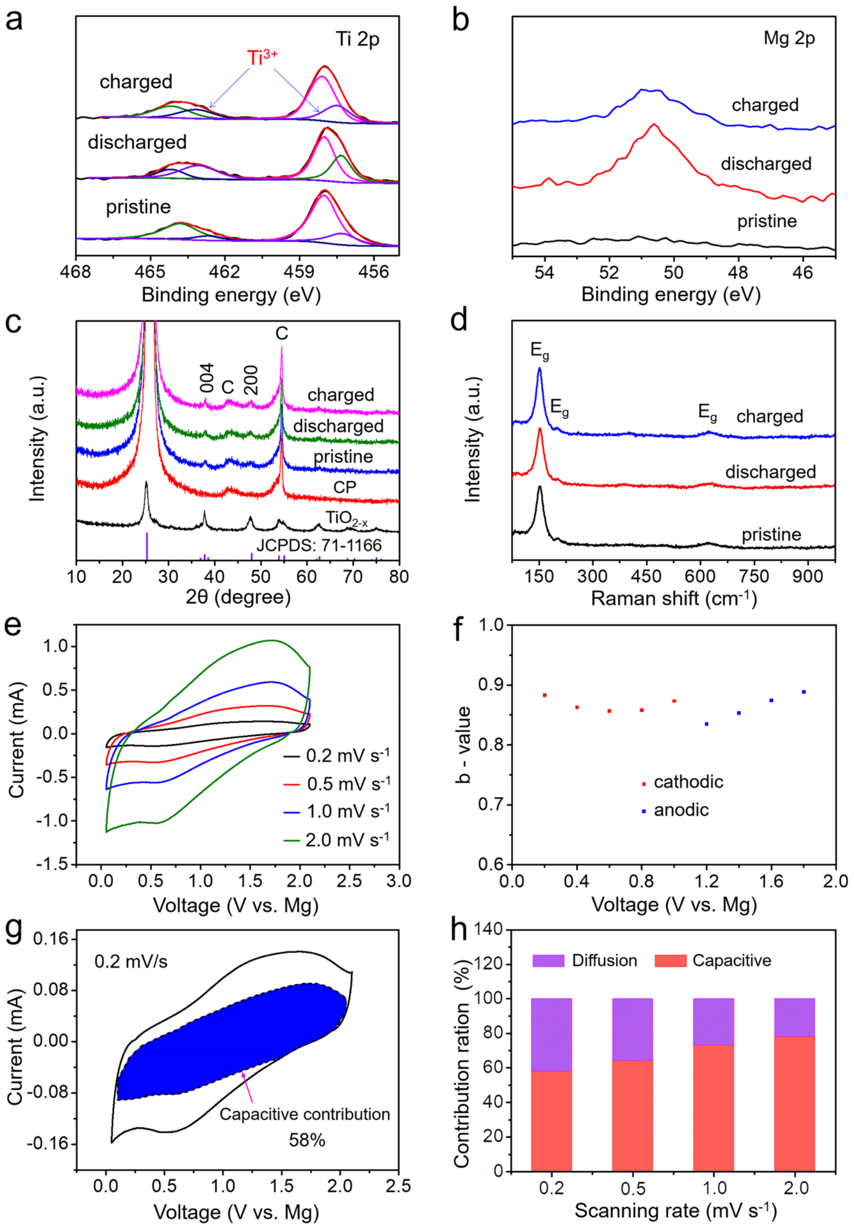

Figure 4. Investigation of the storage mechanism of Mg^{2+} ions in B-TiO_{2-x} nanoflake anode. (a, b) *Ex situ* XPS spectra acquired from freshly prepared, first-time discharged, and first-time charged B-TiO_{2-x} nanoflake anode at (a) Ti 2p and (b) Mg 2p regions, respectively. (c) *Ex situ* XRD patterns and (d) *ex situ* Raman spectra of freshly prepared, first-time discharged, and first-time charged B-TiO_{2-x} nanoflake anode. The peaks labeled by "C" are originated from carbon paper (CP) served as current collector. (e) CV curves of the third cycles at different scanning rates. (f) Calculated *b*-values as a function of voltage from the cathodic and anodic sweeps of B-TiO_{2-x} nanoflake anode. (g) Capacitive contribution (the shaded region) to the total stored charge at 0.2 mV s^{-1} calculated based on the equation: $i(V) = k_1\nu + k_2\nu^{1/2}$. (h) Column graphs of rate-dependent charge storage contributions of B-TiO_{2-x} nanoflakes resulted from Mg^{2+} insertion/diffusion and capacitive processes.

energy band structure induced by OVs in the B-TiO_{2-x} nanoflakes. As shown in Figure 2h, the density functional theory (DFT) calculation results of partial density of states (PDOS) indicate that the VB edge of pristine anatase TiO_2 mainly consists of O 2p states, while the CB is mainly composed of Ti 3d states. After the introduction of OVs into anatase TiO_2 (*i.e.*, B-TiO_{2-x}), the Fermi level is shifted to the CB, and the band gap is narrowed. This rationalizes the improved electron conductivity in B-TiO_{2-x}, which was observed in the experiments.

The electrochemical performances of B-TiO_{2-x} nanoflakes for hosting Mg^{2+} ions were evaluated by assembling 2032 coin-type cells with 0.4 M 2PhMgCl-$AlCl_3$ (termed as APC) in THF solution as the electrolyte and polished Mg foil as the anode material. To examine the compatibility of APC electrolyte for Mg stripping/plating in magnesium battery system, cyclic voltammograms (CV) profile was measured with a three-electrode testing system based on the counter and reference electrodes of magnesium foils, the working electrode of platinum plate, and 0.4 M APC/THF electrolyte (Figure S5). The overpotential for Mg plating is measured to be 0.25 V, and the Coulombic efficiency for Mg stripping/plating is ~100%, indicating the good compatibility of APC/THF electrolyte. The CV curves of B-TiO_{2-x} nanoflakes during the first, second, and fifth cycles at a scan rate of 0.2 mV·s^{-1} are provided in Figure 3a. The electrode of porous B-TiO_{2-x} nanoflakes exhibits broad cathodic and anodic responses. Considering the weak redox peaks and the nearly rectangular shape of the CV curves, the storage mechanism of Mg^{2+} for the B-TiO_{2-x} electrode could have both Mg^{2+} insertion/diffusion contribution and electrocapacitive contribution, which will be discussed in detail below. Noticeably, the current density of B-TiO_{2-x} electrode is evidently higher than that of W-TiO_2 (see Figure S6a), suggesting the significantly improved electrochemical activity due to the presence of OVs. Figure 3b depicts the discharge/charge profiles of porous B-TiO_{2-x} nanoflakes at the first, second, and fifth cycles at a current density of 50 mA g^{-1}. The initial discharge and charge capacities are 190 and 134 mAh g^{-1}, respectively, corresponding to the storage of 0.28 equiv of Mg^{2+} per formula unit ($Mg_{0.28}TiO_{2-x}$) and an initial Coulombic efficiency of 70%. The irreversible capacity in the first cycle could be mainly attributed to the Mg^{2+} ions insertion into irreversible sites,[46,47] and the relatively low initial discharge voltage is ascribed to the large polarization associated with the surface oxide layer on Mg anode.[48] In the eighth cycle, the discharge and charge capacities are 147 and 155 mAh g^{-1}, respectively, with the Coulombic efficiency greatly increased to ~95%, corresponding to an estimated Mg^{2+} storage formula of $Mg_{0.22}TiO_{2-x}$. The cycling performance of B-TiO_{2-x} nanoflakes at 150 mA g^{-1} is shown in Figure 3c. The reversible capacity progressively increases during the initial 30 cycles, reaching discharge and charge capacities of 105 and 108 mAh g^{-1}, respectively, with a Coulombic efficiency of ~103%. The discharge capacity still retains as high as 106 mAh g^{-1} after 200 cycles. Figure 3d,e shows the discharge−charge curves and rate capabilities of B-TiO_{2-x} nanoflakes cycling at different current densities ranging from 50 to 300 mA g^{-1}. The discharge capacities are 150, 126, 114, and 106 mAh g^{-1} at 50, 100, 200, and 300 mA g^{-1}, respectively. The capacity of B-TiO_{2-x} electrode exhibits a retention ratio of 70% when the current density increases from 50 mA g^{-1} to 300 mA g^{-1}. Upon cycling, the charge−discharge curves present sloping characteristics. The Mg^{2+} storage properties of representative Ti-based anodes[22,47,49,50] and metallic anodes[18,51,52] for Mg batteries are listed in Table S1. The average discharge voltage of B-TiO_{2-x} was ~0.5 V *vs* Mg^{2+}/Mg, comparable to other reported Ti-based anode materials for Mg batteries, such as $Li_4Ti_5O_{12}$,[22] cation-deficient anatase TiO_2.[49] Moreover, compared with previously reported metallic anodes of Mg batteries, such as, Bi, Sn, Sb, and their alloys, the cycling stability of B-TiO_{2-x} is superior, due to the absence of generally serious volume expansion of metallic anodes.[18,50,51] The long-term cycling test of B-TiO_{2-x} nanoflakes at 300 mA g^{-1} (Figure 3f) shows initial discharge and charge capacities of 101 and 64 mAh g^{-1}, respectively, with an initial Coulombic efficiency of ~63%. The reversible capacity gradually stabilizes after 30 cycles. The 30th discharge and charge capacities are 98 and 102 mAh g^{-1} with a Coulombic efficiency of about 104%. After 400 cycles at 300 mA g^{-1}, the discharge capacity remains at 77 mAh g^{-1} with a capacity retention of 76%, suggesting good cycling stability.

For comparison, we also investigated the Mg^{2+} storage performances of the control samples. The CV curves and charge−discharge curves of W-TiO_2 nanoflakes (see Figure S6a and S6b) with very few OVs display similar features compared to those of B-TiO_{2-x}. The Mg^{2+} storage performance of other control samples was also examined, as shown in Figure S6c,d. With the increase of annealing time, the control samples show apparently decreased discharge capacities. The long-term cycling curve of W-TiO_2 nanoflakes at 300 mA g^{-1} (see Figure S6d) exhibits initial discharge and charge capacities of merely 35 and 30 mAh g^{-1} at 300 mA g^{-1}, respectively, much lower than B-TiO_{2-x}. Electrochemical impedance spectroscopy (EIS) analysis of B-TiO_{2-x} and W-TiO_2 was conducted (see Figure S7). The semicircles in high-frequency regions of the Nyquist plots are relevant with the charge-transfer resistance (R_{ct}) at the electrode/electrolyte interface. The B-TiO_{2-x} electrode shows lower R_{ct} value than that of W-TiO_2, thus conducive to its Mg^{2+} storage performances. The above results indicate that the porous B-TiO_{2-x} nanoflakes have much better Mg^{2+} storage performance than the control samples prepared by annealing at 450 °C in air, in accordance with the variation of OV contents.

To investigate the storage mechanism of Mg^{2+} ions, *ex situ* XPS, *ex situ* XRD, and *ex situ* Raman spectroscopy were conducted on freshly prepared, first-time discharged, and first-time charged B-TiO_{2-x} nanoflakes (Figure 4a−d). In Figure 4a, the XPS spectrum of freshly prepared B-TiO_{2-x} electrode at Ti 2p region shows four peaks. The peaks located at 458.0 and 463.8 eV correspond to the Ti $2p_{3/2}$ and Ti $2p_{1/2}$ bands of Ti^{4+}, respectively. The other two small peaks centered at 457.3 and 462.7 eV are assigned to the $2p_{3/2}$ and $2p_{1/2}$ peaks of Ti^{3+}, respectively. The proportion of the Ti^{4+} and Ti^{3+} species in B-TiO_{2-x} quantified by the XPS results is about 80% and 20%, respectively, corresponding to a x value of ~0.1 (Table S2). After discharged to 0.05 V, the proportion of Ti^{3+} increases from 20% to 48%. Whereas, after charging to 2.1 V, the proportion of Ti^{3+} quantified by the XPS results decreases to 33%, implying that some Mg^{2+} ions are still trapped in the electrode materials (Table S2). These results clearly suggest that the Ti^{4+}/Ti^{3+} conversion has participated in the discharge−charge processes. The increase of Ti^{3+} concentration in B-TiO_{2-x} can lead to an enhancement in the electronic conductivity and thus decreases polarization in the subsequent cycles, as shown in Figure 3b. The XPS spectra at Mg 2p core levels of the freshly prepared, first-time discharged, first-time charged B-TiO_{2-x} nanoflake anode are shown in Figure 4b. The peak intensity at charged state is lower than that at a discharged state, indicating the reversible magnesiation/demagnesiation of B-TiO_{2-x} nanoflakes, but some Mg^{2+} ions are always trapped in B-TiO_{2-x} throughout the cycling process. The atomic contents of Mg^{2+} after the first discharge and charge steps were also estimated by EDX, as shown in Figure S8a,b, respectively, which is in accordance with the measured battery capacities. Meanwhile, the *ex situ* XRD (Figure 4c) and *ex situ* Raman spectroscopy (Figure 4d) features show no appearance of new peaks and negligible peak shifts upon the magnesiation/demagnesiation process. The XRD and Raman peak intensities also show only slight changes, indicating the good reversibility upon cycling. The CV curves at various scan rates from 0.2 to 2.0 mV s^{-1} were collected to further investigate the electrochemical behavior of B-TiO_{2-x} nanoflakes (Figure 4e), which exhibit broad cathodic and anodic responses. Generally, the current (i) obeys a function relationship with the scan rate (ν) during the sweeps:

$$i(\mathrm{V}) = a\nu^{b} \tag{1}$$

$$\lg i(\mathrm{V}) = b\lg\nu + \lg a \tag{2}$$

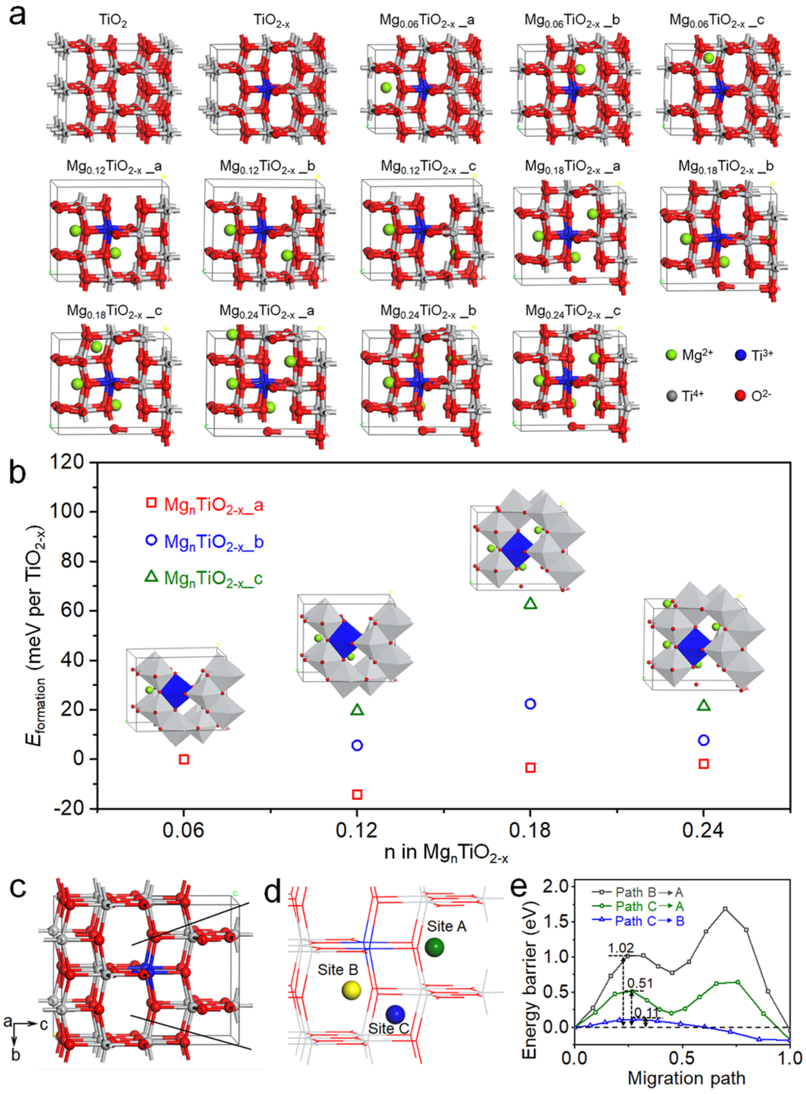

Figure 5. DFT calculations. (a) Structure models of TiO_2 and possible Mg^{2+} insertion sites in Mg_nTiO_{2-x} (n = 0.06, 0.12, 0.18, or 0.24). (b) Calculated formation energies of Mg^{2+} insertion into anatase TiO_{2-x} with different amounts of Mg^{2+} ions. Illustrations of (c) simulation model along with (d) the possible insertion sites A, B, and C for Mg ions. (e) Calculated relative energy curves of three corresponding migration paths for one Mg^{2+} ion in supercell of TiO_{2-x}: Path B → A, Path C → A, and Path C → B.

where the measured current i obeys a power law relationship with the sweep rate (v), and a and b are the adjustable parameters.[53,54] The electrode is diffusion governed if the b-value is 0.5, while the b-value is close to 1.0 indicating that a capacitive response is dominant.[24,55−57] The b-values calculated from the CV curves of B-TiO_{2-x} nanoflakes at various current densities are shown in Figure 4f and Figure S9a,b. During both cathodic and anodic processes, the b-values are in the range of 0.83−0.89, which suggests that both diffusion process and capacitive response contribute to the total stored capacity.[58,59] The fraction of the above-mentioned two contributions at a certain scan rate can be quantified according to the following formula:

$$i(\mathrm{V}) = k_1 v + k_2 v^{1/2} \tag{3}$$

$$i(\mathrm{V}) v^{-1/2} = k_1 v^{1/2} + k_2 \tag{4}$$

where $i(\mathrm{V})$, v, k_1v, and $k_2v^{1/2}$ are the currents at a specific potential, the scanning rate, the capacitive-controlled current, and the diffusion-limited current, respectively. Figure S9c,d shows the linear plots of $i(\mathrm{V})\ v^{-1/2}$ *vs* $v^{1/2}$ at specific voltages during the discharge and charge processes. The capacitive contributions, corresponding to the shaded areas of the CV curves at the scanning rates of 0.2, 0.5, 1.0, and 2.0 mV s^{-1} (Figure 4g and Figure S10), are calculated to be ∼58%, 64%, 73%, and 78% of the total capacities, respectively. The capacitive contribution becomes more prominent along with the increase of scanning rate, as shown in Figure 4h. Similar phenomena have also been reported in other research works on Mg batteries.[60,61]

DFT calculations were performed to further investigate the Mg^{2+} insertion/extraction mechanism of B-TiO_{2-x}, and the computational method is detailed in the Experimental Section. The oxygen vacancy configurations of TiO_{2-x} were created by removing an oxygen atom at the center of the 2 × 2 × 1 anatase TiO_2 supercell, where O was three-fold coordinated to Ti. In the unit cell of TiO_{2-x}, there are three kinds of possible nonequivalent insertion sites for Mg^{2+} (labeled as site A, B, and C), as illustrated in Figure S11. The sites A and B are the octahedral interstitials including a normal (*i.e.*, Ti^{4+}) and a lower oxidation state of Ti (*i.e.*, Ti^{3+}), respectively. The site C is the edge-shared Ti^{4+}-O octahedral interstitial. Figure 5a displays the possible Mg^{2+} insertion states in the TiO_{2-x} unit cell (Mg_nTiO_{2-x}, n = 0.06, 0.12, 0.18, or 0.24). The relative formation energy ($E_{\text{formation}}$) for Mg^{2+} ion insertion into TiO_{2-x} was also calculated, as shown in Table S3. The more negative formation energy means more energy-preferable insertion of Mg^{2+} into the TiO_{2-x}. It is revealed that the Mg insertion at the site A (*i.e.*, $Mg_{0.06}TiO_{2-x}$_a) is most energetically favorable with the lowest energy among the three insertion sites. In contrast, the Mg^{2+} insertion at the site C is very difficult, owing to the higher energy relative to those of sites A and B resulted from the much smaller cavity of the site C (Table S3). Figure 5b shows the absolute values of calculated formation energies in Mg_nTiO_{2-x} changed along with the content of Mg^{2+} ions insertion. It can be seen that the further insertion is energetically favorable when the content of Mg^{2+} in the TiO_{2-x} unit cell is <0.24. Figure 5c and Table S4 indicate that the migration of Mg^{2+} from the energetically less favorable site C ($Mg_{0.06}TiO_{2-x}$_c) to the more stable site B ($Mg_{0.06}TiO_{2-x}$_b) is easiest, corresponding to the smallest migration energy barrier (0.11 eV). This implies that site C is impossible for Mg^{2+} insertion both thermodynamically and kinetically, therefore the Mg^{2+} migration through the Path C → B will not take place in reality, although the energy barrier is low. Furthermore, it is revealed that a longer migration distance usually results in a larger migration energy barrier.

CONCLUSIONS

In summary, we report an efficient atomic substation formation strategy to prepare ultrathin porous B-TiO_{2-x} nanoflakes containing abundant OVs, which play a crucial role in the reversible Mg^{2+} storage with high discharge−charge capacity and long cycle stability. Both experimental results and DFT calculations indicate that the OVs can enhance the electric conductivity and increase the number of active sites Mg^{2+} storage. The OVs-rich ultrathin B-TiO_{2-x} nanoflakes exhibited greatly improved kinetics and capacity for Mg^{2+} ion storage compared with the W-TiO_2 control sample. This work demonstrates the possibility to utilize the defect engineering strategy to improve the overall electrochemical performances of electrode materials for rechargeable Mg batteries.

EXPERIMENTAL SECTION

Synthesis of Ultrathin TiS_2 Nanoflakes. Typically, 800 mg of sulfur was dissolved in 30 mL of oleylamine in a three-neck flask. The solution was first heated to 100 °C under vigorous magnetic stirring with the protection of high-purity nitrogen for about 2 h to remove water and oxygen. The solution was naturally cooled down to room temperature. Afterward, 2 mL of $TiCl_4$ was injected into the flask. The temperature of the solution was gradually raised to 300 °C within 3 h and maintained at 300 °C for another 3 h in nitrogen atmosphere. The products were centrifuged and washed with trichloromethane and absolute alcohol for several times and then dried in a vacuum oven at 60 °C for 12 h. Finally, the product was annealed in Ar atmosphere at 400 °C for 4 h to remove any possible organic residues.

Synthesis of Porous Black TiO_{2-x} (B-TiO_{2-x}) Nanoflakes. Typically, 100 mg of TiS_2 nanoflakes was dispersed in 20 mL of deionized water under vigorous stirring at room temperature for 72 h. Finally, the product was centrifuged and washed with deionized water and absolute alcohol for several times and then dried in a vacuum oven at 50 °C for 12 h.

The control samples with different OV contents were prepared by annealing porous B-TiO_{2-x} nanoflakes at 450 °C in air for different periods (1 h, 2 h, 4 h).

Characterizations. The morphology of samples was investigated by scanning electron microscopy (SEM, HITACH S-4800) and transmission electron microscopy (TEM, JEM-2100). X-ray powder diffraction (XRD) was recorded by using an XRD-6000 diffractometer (Shimadzu Co., Japan), equipped with a rotating anode and a Cu *Kα* radiation source (λ = 1.54178 Å). Nitrogen adsorption−desorption isotherms were measured through Brunauer−Emmett−Teller (BET) model at 77 K on a Quantachrome Autosorb-IQ-2C-TCD-VP instrument. X-ray photoelectron spectra (XPS) were obtained using a PHI-5000 VersaProbe X-ray photoelectron spectrometer with an Al *Kα* X-ray source. The EPR spectra were obtained using a Bruker EMX-10/12 X-band spectrometer at room temperature. UV−vis diffuse reflectance spectra were measured with Shimadzu UV-2600 using $BaSO_4$ powder as the reference sample in the range of 300−1200 nm.

Battery Assembly and Electrochemical Measurements. The working electrode was prepared by using a mixture of 80 wt % of the designated active materials (B-TiO_{2-x} or W-TiO_2), 10 wt % of Ketjenblack, and 10 wt % of polyvinylidene fluoride (PVDF) as binder. The mixture was added to *N*-methyl-2-pyrrolidinone (NMP) solvent to form a homogeneous slurry, which was then spread on carbon paper as the current collector and dried in a vacuum oven at 60 °C for 12 h. The mass loading of active material is about 1.5−2.0 mg cm^{-2}. Coin-type (CR2032) cells were assembled in an argon-filled glovebox with Whatman glass fiber (GF/A) as separators and fresh polished Mg foil as anodes. Mg foil was polished with carbide paper and cleaned with THF solvent prior to use. The THF solution of 0.4 M $2PhMgCl-AlCl_3$ (termed as APC) was used as the electrolyte in Mg batteries, following a previously reported procedure.[62] The galvanostatic charge−discharge experiments were performed on a LAND CT2001A multichannel battery test system between 0.05 and 2.1 V *vs* Mg^{2+}/Mg at room temperature. Cyclic voltammetry (CV) measurement was conducted using an electrochemistry workstation (Chenhua CHI-760E) at a scanning rate of 0.2 mV s^{-1}. The specific capacity was calculated based on the loading mass of active material.

Computational Methods. The DFT calculations were performed using the CASTEP code based on spin-polarized DFT within the generalized gradient approximation (GGA) with the Perdew−Burke−Ernzerhof (PBE) method. The ultrasoft pseudopotential was implemented to describe the interaction between valence electrons and ionic core. The cutoff energy for the plane wave expansion was 380 eV, and the Monkhorst−Pack scheme *k*-point mesh for the Brillouin-zone integration was generated with a 3 × 3 × 3 unit. The geometry optimization was carried out until the total energy and the maximum force were $<1.0 \times 10^{-5}$ eV/atom and 0.03 eV/Å, respectively. For Mg^{2+} insertion systems, a 2 × 2 × 1 anatase TiO_2 supercell with one oxygen vacancy (OV) was utilized. The oxygen vacancy configurations of $Ti_{16}O_{31}$ were created by removing an oxygen atom at the center of the supercell, where O was three-fold coordinated to Ti. For simplicity, $Ti_{16}O_{31}$ model can be expressed as B-TiO_{2-x}. It should be mentioned that the OVs concentration in this model is higher than that was detected in our experiments, however, the qualitative conclusions on the OVs effect on the electronic structures can be satisfactorily drawn from the selected $Ti_{16}O_{31}$ model to rationalize experiments.

In the cell of B-TiO_{2-x}, one Mg ion has three possible nonequivalent insertion sites (labeled as sites A, B, and C) as illustrated in Figure S11. The energy barrier for one Mg^{2+} ion migration inside B-TiO_{2-x} was calculated through a transition-state structure (TS) search strategy using complete LST/QST search protocol and the nudged elastic band (NEB) method. The value of the convergence threshold was set to 0.05 eV/Å.

The relative formation energy ($E_{\text{formation}}$) per TiO_{2-x} unit based on the 2 × 2 × 1 anatase TiO_2 supercell with one OV is defined as

$$E_{\text{formation}} = E(Mg_nTiO_{2-x}) - E(Mg_{n-0.06}TiO_{2-x}) - (E(Mg_{0.06}TiO_{2-x}) - E(TiO_{2-x})) \quad (5)$$

DOI: 10.1021/acsnano.8b06917
ACS Nano 2018, 12, 12492−12502

where n is the content of Mg^{2+} ions insertion, $E(Mg_nTiO_{2-x})$ is the energy with n Mg^{2+} ions insertion into the anatase B-TiO_{2-x}, and $E(TiO_{2-x})$ is the energy of the 2 × 2 × 1 anatase TiO_2 supercell with one OV.

ASSOCIATED CONTENT

Supporting Information

The Supporting Information is available free of charge on the ACS Publications website at DOI: 10.1021/acsnano.8b06917.

> Figures S1−S11 and Tables S1−S4; XRD pattern of TiS_2 nanoflakes; SEM and HRTEM images of W-TiO_2 nanoflakes; BET, XPS, EDX, and EIS analysis results; CV curve of electrolyte; electrochemical investigations of control samples; investigation of Mg^{2+} ions storage mechanism; DFT calculation details; performance comparison with other anode materials for Mg batteries (PDF)

AUTHOR INFORMATION

Corresponding Authors

*E-mail: majing@nju.edu.cn.
*E-mail: zhongjin@nju.edu.cn.

ORCID

Tao Chen: 0000-0003-2536-4145
Jing Ma: 0000-0001-5848-9775
Jie Liu: 0000-0003-0451-6111
Zhong Jin: 0000-0001-8860-8579

Notes

The authors declare no competing financial interest.

ACKNOWLEDGMENTS

This work was supported by National Key R&D Program of China (2017YFA0208200, 2016YFB0700600, 2015CB659300), Projects of NSFC (21872069, 51761135104, 21573108), Natural Science Foundation of Jiangsu Province (BK20180008, BK20150583), High-Level Entrepreneurial and Innovative Talents Program of Jiangsu Province, and the Fundamental Research Funds for the Central Universities of China (020514380146). We are also grateful to the High Performance Computing Centre of Nanjing University for providing the IBM Blade cluster system.

REFERENCES

(1) Ponrouch, A.; Frontera, C.; Bardé, F.; Palacín, M. R. Towards a Calcium-Based Rechargeable Battery. *Nat. Mater.* **2016**, *15*, 169−172.

(2) Aurbach, D.; Suresh, G. S.; Levi, E.; Mitelman, A.; Mizrahi, O.; Chusid, O.; Brunelli, M. Progress in Rechargeable Magnesium Battery Technology. *Adv. Mater.* **2007**, *19*, 4260−4267.

(3) Lin, M. C.; Gong, M.; Lu, B. G.; Wu, Y. P.; Wang, D. Y.; Guan, M. Y.; Angell, M.; Chen, C. X.; Yang, J.; Hwang, B. J.; Dai, H. J. An Ultrafast Rechargeable Aluminium-Ion Battery. *Nature* **2015**, *520*, 324−328.

(4) Wang, Y. R.; Chen, R. P.; Chen, T.; Lv, H. L.; Zhu, G. Y.; Ma, L. B.; Wang, C. X.; Jin, Z.; Liu, J. Emerging Non-Lithium Ion Batteries. *Energy Storage Mater.* **2016**, *4*, 103−129.

(5) Bucur, C. B.; Gregory, T.; Oliver, A. G.; Muldoon, J. Confession of a Magnesium Battery. *J. Phys. Chem. Lett.* **2015**, *6*, 3578−3591.

(6) Yoo, H.; Shterenberg, I.; Gofer, Y.; Gershinsky, G.; et al. Mg Rechargeable Batteries: an On-Going Challenge. *Energy Environ. Sci.* **2013**, *6*, 2265−2279.

(7) Muldoon, J.; Bucur, C. B.; Oliver, A. G.; Sugimoto, T.; Matsui, M.; Kim, H. S.; Allred, G. D.; Zajicek, J.; Kotani, Y. Electrolyte Roadblocks to a Magnesium Rechargeable Battery. *Energy Environ. Sci.* **2012**, *5*, 5941−5950.

(8) Sun, X. Q.; Bonnick, P.; Duffort, V.; Liu, M.; Rong, Z. Q.; Persson, K. A.; Ceder, G.; Nazar, L. F. A High Capacity Thiospinel Cathode for Mg Batteries. *Energy Environ. Sci.* **2016**, *9*, 2273−2277.

(9) Sun, X. Q.; Bonnick, P.; Nazar, L. F. Layered TiS_2 Positive Electrode for Mg Batteries. *ACS Energy Lett.* **2016**, *1*, 297−301.

(10) Aurbach, D.; Lu, Z.; Schechter, A.; Gofer, Y.; Gizbar, H.; Turgeman, R.; Cohen, Y.; Moshkovich, M.; Levi, E. Prototype Systems for Rechargeable Magnesium Batteries. *Nature* **2000**, *407*, 724−727.

(11) Saha, P.; Datta, M. K.; Velikokhatnyi, O. I.; Manivannan, A.; Alman, D.; Kumta, P. N. Rechargeable Magnesium Battery: Current Status and Key Challenges for the Future. *Prog. Mater. Sci.* **2014**, *66*, 1−86.

(12) Kim, C.; Phillips, P. J.; Key, B.; Yi, T.; Nordlund, D.; Yu, Y. S.; Bayliss, R. D.; Han, S. D.; He, M. N.; Zhang, Z. C.; Burrell, A. K.; Klie, R. F.; Cabana, J. Direct Observation of Reversible Magnesium Ion Intercalation Into a Spinel Oxide Host. *Adv. Mater.* **2015**, *27*, 3377−3384.

(13) Arthur, T. S.; Kato, K.; Germain, J.; Guo, J. H.; Glans, P.; Liu, Y. S.; Holmes, D.; Fan, X. D.; Mizuno, F. Amorphous V_2O_5−P_2O_5 as High-Voltage Cathodes for Magnesium Batteries. *Chem. Commun.* **2015**, *51*, 15657−15660.

(14) Tepavcevic, S.; Liu, Y. Z.; Zhou, D. H.; Lai, B.; Maser, J.; Zuo, X. B.; Chan, H.; Kral, P.; Johnson, C. S.; Stamenkovic, V.; Markovic, N. M.; Rajh, T. Nanostructured Layered Cathode for Rechargeable Mg-Ion Batteries. *ACS Nano* **2015**, *9*, 8194−8205.

(15) Pour, N.; Gofer, Y.; Major, D. T.; Aurbach, D. Structural Analysis of Electrolyte Solutions for Rechargeable Mg Batteries by Stereoscopic Means and DFT Calculations. *J. Am. Chem. Soc.* **2011**, *133*, 6270−6278.

(16) Tutusaus, O.; Mohtadi, R.; Arthur, T. S.; Mizuno, F.; Nelson, E.; Sevryugina, Y. V. An Efficient Halogen−Free Electrolyte for Use in Rechargeable Magnesium Batteries. *Angew. Chem., Int. Ed.* **2015**, *54*, 7900−7904.

(17) Zhou, X. J.; Tian, J.; Hu, J. L.; Li, C. L. High Rate Magnesium-Sulfur Battery with Improved Cyclability Based on Metal-Organic Framework Derivative Carbon Host. *Adv. Mater.* **2018**, *30*, 1704166.

(18) Cheng, Y. W.; Shao, Y. Y.; Parent, L. R.; Sushko, M. L.; Li, G. S.; Sushko, P. V.; Browning, N. D.; Wang, C. M.; Liu, J. Interface Promoted Reversible Mg Insertion in Nanostructured Tin−Antimony Alloys. *Adv. Mater.* **2015**, *27*, 6598−6605.

(19) Shao, Y. Y.; Gu, M.; Li, X. L.; Nie, Z. M.; Zuo, P. J.; Li, G. S.; Liu, T. B.; Xiao, J.; Cheng, Y. W.; Wang, C. M.; Zhang, J. G.; Liu, J. Highly Reversible Mg Insertion in Nanostructured Bi for Mg Ion Batteries. *Nano Lett.* **2014**, *14*, 255−260.

(20) Singh, N.; Arthur, T. S.; Ling, C.; Matsui, M.; Mizuno, F. A high Energy-Density Tin Anode for Rechargeable Magnesium-Ion Batteries. *Chem. Commun.* **2013**, *49*, 149−151.

(21) Wang, Z.; Su, Q.; Shi, J.; Deng, H.; Yin, G. Q.; Guan, J.; Wu, M. P.; Zhou, Y. L.; Lou, H. L.; Fu, Y. Q. Comparison of Tetragonal and Cubic Tin as Anode for Mg Ion Batteries. *ACS Appl. Mater. Interfaces* **2014**, *6*, 6786−6789.

(22) Wu, N.; Lyu, Y. C.; Xiao, R. J.; Yu, X. Q.; Yin, Y. X.; Yang, X. Q.; Li, H.; Guo, Y. G. A Highly Reversible, Low-Strain Mg-Ion Insertion Anode Material for Rechargeable Mg-Ion Batteries. *NPG Asia Mater.* **2014**, *6*, e120.

(23) Wu, N.; Yang, Z. Z.; Yao, H. R.; Yin, Y. X.; Gu, L.; Guo, Y. G. Improving the Electrochemical Performance of the $Li_4Ti_5O_{12}$ Electrode in a Rechargeable Magnesium Battery by Lithium−Magnesium Co-Intercalation. *Angew. Chem.* **2015**, *127*, 5849−5853.

(24) Kim, H.; Cook, J. B.; Lin, H.; Ko, J. S.; Tolbert, S. H.; Ozolins, V.; Dunn, B. Oxygen Vacancies Enhance Pseudocapacitive Charge Storage Properties of MoO_{3-x}. *Nat. Mater.* **2017**, *16*, 454−460.

(25) Schaub, R.; Wahlstrçm, E.; Rønnau, A.; Lægsgaard, E.; Stensgaard, I.; Besenbacher, F. Oxygen-Mediated Diffusion of Oxygen Vacancies on the TiO_2 (110) Surface. *Science* **2003**, *299*, 377−379.

(26) Chen, X. B.; Liu, L.; Yu, P. Y.; Mao, S. S. Increasing Solar Absorption for Photocatalysis with Black Hydrogenated Titanium Dioxide Nanocrystals. *Science* **2011**, *331*, 746−750.

(27) Levasseur, S.; Ménétrier, M.; Horn, Y. S.; Gautier, L.; Audemer, A.; Demazeau, G.; Largeteau, A.; Delmas, C. Oxygen Vacancies and Intermediate Spin Trivalent Cobalt Ions in Lithium-Overstoichiometric $LiCoO_2$. *Chem. Mater.* **2003**, *15*, 348−354.

(28) Lu, X. H.; Wang, G. M.; Zhai, T.; Yu, M. H.; Gan, J. Y.; Tong, Y. X.; Li, Y. Hydrogenated TiO_2 Nanotube Arrays for Supercapacitors. *Nano Lett.* **2012**, *12*, 1690−1696.

(29) Zhang, Y.; Ding, Z. Y.; Foster, C. W.; Banks, C. E.; Qiu, X. Q.; Ji, X. B. Oxygen Vacancies Evoked Blue TiO_2(B) Nanobelts with Efficiency Enhancement in Sodium Storage Behaviors. *Adv. Funct. Mater.* **2017**, *27*, 1700856.

(30) Song, J.; Shin, D. W.; Lu, Y. H.; Amos, C. D.; Manthiram, A.; Goodenough, J. B. Role of Oxygen Vacancies on the Performance of $Li[Ni_{0.5-x}Mn_{1.5+x}]O_4$ (x = 0, 0.05, and 0.08) Spinel Cathodes for Lithium-Ion Batteries. *Chem. Mater.* **2012**, *24*, 3101−3109.

(31) Xia, T.; Zhang, W.; Murowchick, J. B.; Liu, G.; Chen, X. B. A Facile Method to Improve the Photocatalytic and Lithium-Ion Rechargeable Battery Performance of TiO_2 Nanocrystals. *Adv. Energy Mater.* **2013**, *3*, 1516−1523.

(32) Sushko, P. V.; Rosso, K. M.; Zhang, J. G.; Liu, J.; Sushko, M. L. Oxygen Vacancies and Ordering of d-levels Control Voltage Suppression in Oxide Cathodes: the Case of Spinel $LiNi_{0.5}Mn_{1.5}O_{4-\delta}$. *Adv. Funct. Mater.* **2013**, *23*, 5530−5535.

(33) Xu, Y.; Zhou, M.; Wang, X.; Wang, C. L.; Liang, L. Y.; Grote, F. B.; Wu, M. H.; Mi, Y.; Lei, Y. Enhancement of Sodium Ion Battery Performance Enabled by Oxygen Vacancies. *Angew. Chem., Int. Ed.* **2015**, *54*, 8768−8771.

(34) Brezesinski, T.; et al. Ordered Mesoporous α-MoO_3 with Iso-Oriented Nanocrystalline Walls for Thin-Film Pseudocapacitors. *Nat. Mater.* **2010**, *9*, 146−151.

(35) Lu, X.; Chen, A.; Luo, Y.; Lu, P.; Dai, Y.; Enriquez, E.; Dowden, P.; Xu, H.; Kotula, P. G.; Azad, A. K.; Yarotski, D. A.; Prasankumar, R. P.; Taylor, A. J.; Thompson, J. D.; Jia, Q. Conducting Interface in Oxide Homojunction: Understanding of Superior Properties in Black TiO_2. *Nano Lett.* **2016**, *16*, 5751−5755.

(36) Zhou, W.; Li, W.; Wang, J. Q.; Qu, Y.; Yang, Y.; Xie, Y.; Zhang, K. F.; Wang, L.; Fu, H. G.; Zhao, D. Y. Ordered Mesoporous Black TiO_2 as Highly Efficient Hydrogen Evolution Photocatalyst. *J. Am. Chem. Soc.* **2014**, *136*, 9280−9283.

(37) Liu, N.; Schneider, C.; Freitag, D.; Hartmann, M.; Venkatesan, U.; Müller, J.; Spiecker, E.; Schmuki, P. Black TiO_2 Nanotubes: Cocatalyst-Free Open-Circuit Hydrogen Generation. *Nano Lett.* **2014**, *14*, 3309−3313.

(38) Chen, C. J.; Wen, Y. W.; Hu, X. L.; Ji, X. L.; Yan, M. Y.; Mai, L. Q.; Hu, P.; Shan, B.; Huang, Y. H. Na^+ Intercalation Pseudocapacitance in Graphene-Coupled Titanium Oxide Enabling Ultra-Fast Sodium Storage and Long-Term Cycling. *Nat. Commun.* **2015**, *6*, 6929−6936.

(39) Tan, H. Q.; Zhao, Z.; Niu, M.; Mao, C. Y.; Cao, D. P.; Cheng, D. J.; Feng, P. Y.; Sun, Z. C. A Facile and Versatile Method for Preparation of Colored TiO_2 with Enhanced Solar-Driven Photocatalytic Activity. *Nanoscale* **2014**, *6*, 10216−10223.

(40) Naldoni, A.; Allieta, M.; Santangelo, S.; Marelli, M.; Fabbri, F.; Cappelli, S.; Bianchi, C. L.; Psaro, R.; Dal Santo, V. Effect of Nature and Location of Defects on Bandgap Narrowing in Black TiO_2 Nanoparticles. *J. Am. Chem. Soc.* **2012**, *134*, 7600−7603.

(41) D'Arienzo, M.; Carbajo, J.; Bahamonde, A.; Crippa, M.; Polizzi, S.; Scotti, R.; Wahba, L.; Morazzoni, F. Photogenerated Defects in Shape-Controlled TiO_2 Anatase Nanocrystals: A Probe to Evaluate the Role of Crystal Facets in Photocatalytic Processes. *J. Am. Chem. Soc.* **2011**, *133*, 17652−17661.

(42) Gopal, N. O.; Lo, H. H.; Sheu, S. C.; Ke, S. C. A Potential Site for Trapping Photogenerated Holes on Rutile TiO_2 Surface as Revealed by EPR Spectroscopy: An Avenue for Enhancing Photocatalytic Activity. *J. Am. Chem. Soc.* **2010**, *132*, 10982−10983.

(43) Zou, X. X.; Liu, J. K.; Su, J.; Zuo, F.; Chen, J. S.; Feng, P. Y. Facile Synthesis of Thermal and Photostable Titania with Paramagnetic Oxygen Vacancies for Visible Light Photocatalysis. *Chem. - Eur. J.* **2013**, *19*, 2866−2873.

(44) Cui, H. L.; Zhao, W.; Yang, C. Y.; Yin, H.; Lin, T. Q.; Shan, Y. F.; Xie, Y.; Gu, H.; Huang, F. Q. Black TiO_2 Nanotube Arrays for High-Efficiency Photoelectrochemical Water-Splitting. *J. Mater. Chem. A* **2014**, *2*, 8612−8616.

(45) Shen, L. Y.; Xing, Z. P.; Zou, J. L.; Li, Z. Z.; Wu, X. Y.; Zhang, Y. C.; Zhu, Q.; Yang, S. L.; Zhou, W. Black TiO_2 Nanobelts/g-C_3N_4 Nanosheets Laminated Heterojunctions with Efficient Visible-Light-Driven Photocatalytic Performance. *Sci. Rep.* **2017**, *7*, 41978−41988.

(46) Su, S. J.; Huang, Z. G.; NuLi, Y. N.; Tuerxun, F.; Yang, J.; Wang, J. L. A novel Rechargeable Battery with a Magnesium Anode, A Titanium Dioxide Cathode, and A Magnesium Borohydride/Tetraglyme Electrolyte. *Chem. Commun.* **2015**, *51*, 2641−2644.

(47) Meng, Y.; Wang, D. S.; Zhao, Y. Y.; Lian, R. Q.; Wei, Y. J.; Bian, X. F.; Gao, Y.; Du, F.; Liu, B. B.; Chen, G. Ultrathin TiO_2-B Nanowires as an Anode Material for Mg-Ion Batteries Based on a Surface Mg Storage Mechanism. *Nanoscale* **2017**, *9*, 12934−12940.

(48) Ha, S. Y.; Lee, Y. W.; Woo, S. W.; Koo, B.; Kim, J. S.; Cho, J.; Lee, K. T.; Choi, N. S. Magnesium(II) Bis(Trifluoromethane Sulfonyl) Imide-Based Electrolytes with Wide Electrochemical Windows for Rechargeable Magnesium Batteries. *ACS Appl. Mater. Interfaces* **2014**, *6*, 4063−4073.

(49) Koketsu, T.; Ma, J. W.; Morgan, B. J.; Body, M.; Legein, C.; Dachraoui, W.; Giannini, M.; Demortière, A.; Salanne, M.; Dardoize, F.; Groult, H.; Borkiewicz, O. J.; Chapman, K. W.; Strasser, P.; Dambournet, D. Reversible Magnesium and Aluminium Ions Insertion in Cation-Deficient Anatase TiO_2. *Nat. Mater.* **2017**, *16*, 1142−1148.

(50) Chen, C. C.; Wang, J. B.; Zhao, Q.; Wang, Y. J.; Chen, J. Layered $Na_2Ti_3O_7/MgNaTi_3O_7/Mg_{0.5}NaTi_3O_7$ Nanoribbons as High-Performance Anode of Rechargeable Mg-Ion Batteries. *ACS Energy Lett.* **2016**, *1*, 1165−1172.

(51) Arthur, T. S.; Singh, N.; Matsui, M. Electrodeposited Bi, Sb and $Bi_{1-x}Sb_x$ Alloys as Anodes for Mg-Ion Batteries. *Electrochem. Commun.* **2012**, *16*, 103−106.

(52) Parent, L. R.; Cheng, Y.; Sushko, P. V.; Shao, Y.; Liu, J.; Wang, C. M.; Browning, N. D. Realizing the Full Potential of Insertion Anodes for Mg-Ion Batteries Through the Nanostructuring of Sn. *Nano Lett.* **2015**, *15*, 1177−1182.

(53) Brezesinski, T.; Wang, J.; Polleux, J.; Dunn, B.; Tolbert, S. H. Templated Nanocrystal-Based Porous TiO_2 Films for Next-Generation Electrochemical Capacitors. *J. Am. Chem. Soc.* **2009**, *131*, 1802−1809.

(54) Augustyn, V.; Come, J.; Lowe, M. A.; Kim, J. W.; Taberna, P. L.; Tolbert, S. H.; Abruña, H. D.; Simon, P.; Dunn, B. High-Rate Electrochemical Energy Storage Through Li^+ Intercalation Pseudocapacitance. *Nat. Mater.* **2013**, *12*, 518−522.

(55) Augustyn, V.; Simon, P.; Dunn, B. Pseudocapacitive Oxide Materials for High-Rate Electrochemical Energy Storage. *Energy Environ. Sci.* **2014**, *7*, 1597−1614.

(56) Yu, P. F.; Li, C. L.; Guo, X. X. Sodium Storage and Pseudocapacitive Charge in Textured $Li_4Ti_5O_{12}$ Thin Films. *J. Phys. Chem. C* **2014**, *118*, 10616−16024.

(57) Zhu, K.; Wang, Q.; Kim, J. H.; Pesaran, A. A.; Frank, A. J. Pseudocapacitive Lithium-Ion Storage in Oriented Anatase TiO_2 Nanotube Arrays. *J. Phys. Chem. C* **2012**, *116*, 11895−11899.

(58) Wang, P. Y.; Wang, R. T.; Lang, J. E.; Zhang, X.; Chen, Z. K.; Yan, X. B. Porous Niobium Nitride as a Capacitive Anode Material for Advanced Li-Ion Hybrid Capacitors with Superior Cycling Stability. *J. Mater. Chem. A* **2016**, *4*, 9760−9766.

(59) Cao, K. Z.; Jiao, L. F.; Liu, Y. C.; Liu, H. Q.; Wang, Y. J.; Yuan, H. T. Ultra-High Capacity Lithium-Ion Batteries with Hierarchical CoO Nanowire Clusters as Binder Free Electrodes. *Adv. Funct. Mater.* **2015**, *25*, 1082−1089.

(60) Xu, M.; Lei, S. L.; Qi, J.; Dou, Q. Y.; Liu, L. Y.; Lu, Y. L.; Huang, Q.; Shi, S. Q.; Yan, X. B. Opening Magnesium Storage

Capability of Two-Dimensional MXene by Intercalation of Cationic Surfactant. *ACS Nano* **2018**, *12*, 3733−3740.

(61) Wang, L.; Jiang, B.; Vullum, P. E.; Svensson, A. M.; Erbe, A.; Selbach, S. M.; Xu, H. L.; Vullum-Bruer, F. High Interfacial Charge Storage Capability of Carbonaceous Cathodes for Mg Batteries. *ACS Nano* **2018**, *12*, 2998−3009.

(62) Mizrahi, O.; Amir, N.; Pollak, E.; Chusid, O.; Marks, V.; Gottlieb, H.; Larush, L.; Zinigrad, E.; Aurbach, D. Electrolyte Solutions with a Wide Electrochemical Window for Rechargeable Magnesium Batteries. *J. Electrochem. Soc.* **2008**, *155*, A103−A109.